nature nanotechnology

Article

https://doi.org/10.1038/s41565-025-01872-w

Switching on and off the spin polarization of the conduction band in antiferromagnetic bilayer transistors

Received: 2 August 2024

Accepted: 7 January 2025

Published online: 11 March 2025

Check for updates

Fengrui Yao[1,2,7] ✉, Menghan Liao[1,2,7], Marco Gibertini[3,4] ✉, Cheol-Yeon Cheon[1,2], Xiaohanwen Lin[1,2], Fan Wu[1,2], Kenji Watanabe[5], Takashi Taniguchi[6], Ignacio Gutiérrez-Lezama[1,2] & Alberto F. Morpurgo[1,2] ✉

Antiferromagnetic conductors with suitably broken spatial symmetries host spin-polarized bands, which lead to transport phenomena commonly observed in metallic ferromagnets. In bulk materials, it is the given crystalline structure that determines whether symmetries are broken and spin-polarized bands are present. Here we show that, in the two-dimensional limit, an electric field can control the relevant symmetries. To this end, we fabricate a double-gate transistor based on bilayers of van der Waals antiferromagnetic semiconductor $CrPS_4$ and show how a perpendicular electric displacement field can switch the spin polarization of the conduction band on and off. Because conduction band states with opposite spin polarizations are hosted in the different layers and are spatially separated, these devices also give control over the magnetization of the electrons that are accumulated electrostatically. Our experiments show that double-gated $CrPS_4$ transistors provide a viable platform to create gate-induced conductors with near unity spin polarization at the Fermi level, as well as devices with a full electrostatic control of the total magnetization of the system.

In antiferromagnetic conductors, spin order breaks time-reversal ($\hat{T}$) symmetry. However, if a time-reversal symmetry transformation followed by spatial inversion ($\hat{P}$) or by a translation remains a symmetry (so-called crystal time-reversal symmetry), antiferromagnets can behave as if $\hat{T}$ symmetry was effectively present[1–5]. These considerations are key for antiferromagnetic spintronics[6–9], since the breaking of such 'effective' time-reversal symmetry causes physical phenomena characteristic of ferromagnets (anomalous Hall effect[10–13], spin-polarized bands[14–17] and so on), despite the absence of a net magnetization. Identifying bulk antiferromagnets that exhibit these phenomena requires a detailed analysis of the crystalline and magnetic structures, to determine whether $\hat{T}$ symmetry is effectively broken[2,10]. Symmetry considerations analogous to the ones just mentioned are leading to unanticipated results, such as the discovery of altermagnetic compounds[3,4,13,16,17], and are responsible for the rapid development of antiferromagnetic spintronics.

It has been proposed that in some two-dimensional (2D) antiferromagnetic semiconductors[18–23], spatial symmetries can be

[1]Department of Quantum Matter Physics, University of Geneva, Geneva, Switzerland. [2]Group of Applied Physics, University of Geneva, Geneva, Switzerland. [3]Dipartimento di Scienze Fisiche, Informatiche e Matematiche, University of Modena and Reggio Emilia, Modena, Italy. [4]Centro S3, CNR-Istituto Nanoscienze, Modena, Italy. [5]Research Center for Electronic and Optical Materials, National Institute for Materials Science, Tsukuba, Japan. [6]Research Center for Materials Nanoarchitectonics, National Institute for Materials Science, Tsukuba, Japan. [7]These authors contributed equally: Fengrui Yao, Menghan Liao. ✉e-mail: fengrui.yao@unige.ch; marco.gibertini@unimore.it; alberto.morpurgo@unige.ch

https://doi.org/10.1038/s41565-025-01872-w

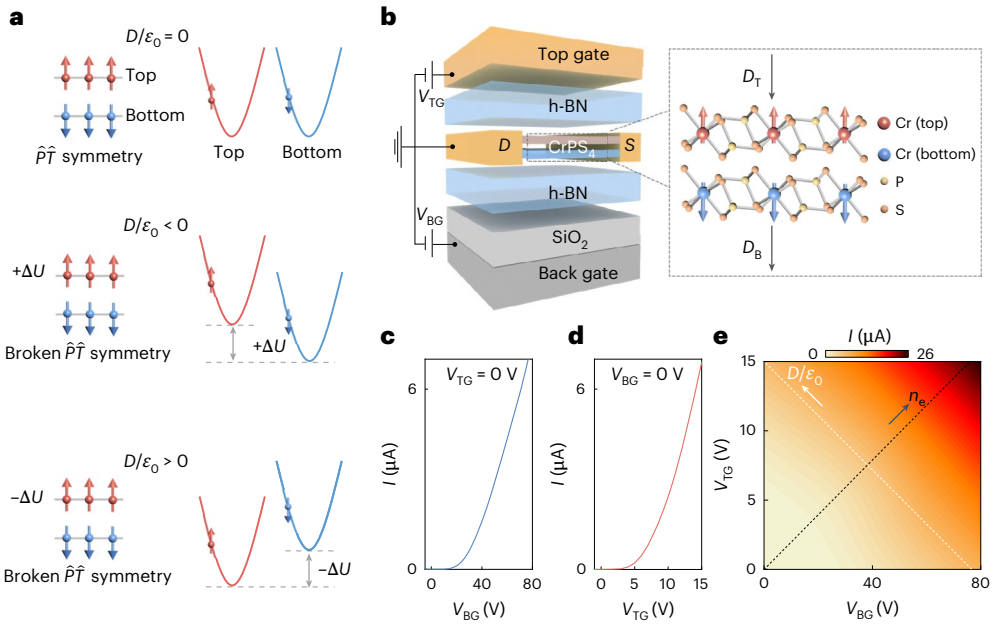

Fig. 1 | Switching spin-polarized bands in A-type antiferromagnetic bilayers (2L). a, Schematics of the low-energy band structure. An A-type antiferromagnetic bilayer hosts switchable spin-up (-down) bands, located in separate layers. The red (blue) spin-up (-down) bands represent the dispersion relation of states in the top (bottom) layer. At zero displacement field ($D/\varepsilon_0 = 0$, top panel), the potential difference ΔU between the layers vanishes, and the spin-up and -down bands are degenerate. At finite ΔU ($D/\varepsilon_0 \neq 0$, middle and bottom panels), the interlayer potential difference lowers the energy of states in one layer (hence with one spin polarity) relative to the other, thereby breaking inversion ($\hat{P}$) and space-time ($\hat{P}\hat{T}$) symmetry. Reversing the sign of D/ε_0 lowers the energy of states located in the other layer (bottom panel), with opposite spin (Supplementary Fig. 1). **b**, Schematic representation of a double-gated $CrPS_4$ bilayer transistor of the type used in this work (see Methods for fabrication details). The zoom-in panel shows a side view of the $CrPS_4$ crystal structure (the red, blue, yellow and orange balls represent top-layer Cr, bottom-layer Cr, P and S atoms, respectively). The double-gated geometry enables independent control of the electron density (n_e) and displacement field ($D/\varepsilon_0 = (D_T + D_B)/2\varepsilon_0$; D_T (D_B) is the displacement field generated by the top (bottom) gate). **c**, Source (S)–drain (D) current I measured in the transistor as a function of top-gate voltage V_{TG} (transfer curve) at fixed back-gate voltage $V_{BG} = 0$. **d**, Transfer curve measured as a function of V_{BG} for $V_{TG} = 0$. **e**, Colour plot of I as a function of V_{BG} and V_{TG}. The black (white) dotted line corresponds to a constant density (displacement) profile. Data shown in this figure were measured at $V_{SD} = 2$ V and at 2 K.

controlled experimentally enabling switching on and off at will the effect of time-reversal symmetry[24–28]. This is the case for bilayers of A-type antiferromagnetic semiconductors, in which the magnetization of one layer is equal and opposite to that of the other layer. Their low-energy conduction band is formed by spin-degenerate states residing in either one of the two layers, whose spin direction is determined by the magnetization of the corresponding layer. The conduction band therefore consists of spin-unpolarized bands, associated to spatially separated electronic states. Under a perpendicular electric displacement field (D), inversion and space-time symmetry are broken, as the interlayer electrostatic potential difference shifts states with one spin to energies lower than states with the opposite spin (Fig. 1a and Supplementary Note 1). The conduction band becomes spin-polarized, and the spin polarization can be reversed by inverting D.

The spatial separation of spin-split bands also gives control over their electronic population by using double-gate field-effect transistors (FETs) that allow tuning independently D and the accumulated charge density (n_e)[29–33]. At zero electric field ($D/\varepsilon_0 = 0$), the potential of the two layers is the same, so that spin-up and -down bands are equally populated (Supplementary Fig. 1 and Supplementary Note 1). When the two gate electrodes are biased asymmetrically, the bands in the two layers shift to different energies. At low n_e, the added electrons go to the layer hosting the lowest conduction band edge and are fully spin-polarized. Here we investigate experimentally double-gated FETs based on $CrPS_4$ antiferromagnetic bilayers (see Fig. 1b and Extended Data Fig. 1 for the schematics of such a device) to controllably generate and populate gate-tunable spin-split bands, and to detect them by measurements of hysteretic magnetoconductance.

Double-gated bilayer $CrPS_4$ transistors

$CrPS_4$ is a weakly anisotropic A-type van der Waals semiconducting antiferromagnet with Néel temperature $T_N = 38$ K (refs. 34–39). Bulk crystals exhibit spin-flip and spin-flop transitions respectively at 7–8 T and 0.6–0.8 T (exact values depend on the crystals investigated). In thick $CrPS_4$ multilayers single-gate FETs, magnetoconductance measurements[38,39] have allowed detecting the influence of the magnetic state on the band structure. In bilayers, electronic structure calculations (Supplementary Fig. 1) show that conduction band states with opposite spin are spatially separated (as needed to create spin polarization by applying a perpendicular electric field). So far, however, no transport measurements have been reported on double-gate bilayer transistors of $CrPS_4$, or of any antiferromagnet (pioneering work on CrI_3 bilayers focused on magneto-optical studies[31–33], because the insulating behaviour of CrI_3 prevented transport measurements[40]).

Figure 1c,d shows transfer curves of a double-gate bilayer $CrPS_4$ device (for thickness identification, see Extended Data Fig. 2) measured as a function of voltage applied to the top and bottom gate. Two-terminal measurements are performed using exfoliated graphite strips as contacts. On thick multilayers, we succeeded in realizing multiterminal transistors showing that two- and four-terminal measurements give virtually identical results at large source–drain bias[41] (these multiterminal devices also show the absence of Hall effect, as it often happens in accumulation layers of low-mobility semiconductors[42]).

Doping-dependent magnetism at zero electric displacement field

Creating and probing spin polarization is effectively achieved by operating double-gate transistors to have large perpendicular electric

https://doi.org/10.1038/s41565-025-01872-w

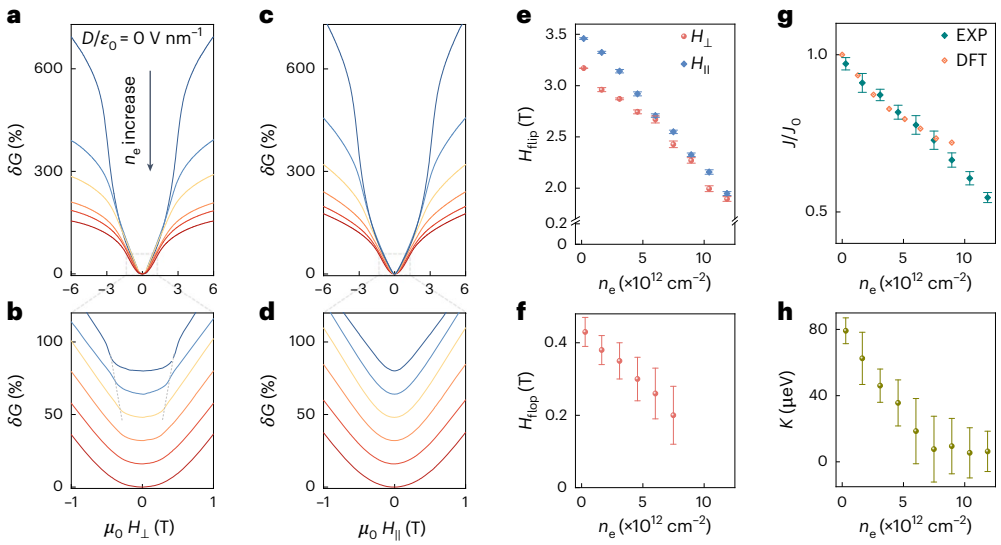

Fig. 2 | Doping-dependent magnetism in 2L $CrPS_4$ at zero displacement field. **a**, Magnetoconductance δG measured at 2 K and zero D/ε_0 as a function of out-of-plane magnetic field $H_\perp$, for n_e varying from 1.75×10^{11} to 1.2×10^{13} cm^{-2}. The field at which δG starts to flatten corresponds to the spin-flip field (H_{flip}) and can be precisely determined from the minimum in the second derivative of conductance (G) with respect to $H_\perp$ (**c**). **b**, Low-field magnetoconductance measured under $H_\perp$, showing the effect of the spin-flop field (H_{flop}, indicated by the dash grey line; H_{flop} is determined by the position of the corresponding peak in d^2G/dH^2). **c**, δG measured under the same conditions as in **a**, with field $H_\parallel$ applied parallel to the plane. **d**, Low-field magnetoconductance measured under $H_\parallel$; as expected, the spin-flop transition is absent. **e**, Evolution of H_{flip} (obtained from the minimum in d^2G/dH^2; Supplementary Fig. 2) for $H_\perp$ and $H_\parallel$ (red and blue dots, respectively) as a function of n_e. H_{flip} is slightly smaller when the field is applied perpendicular to the plane (**e**), because of the uniaxial magnetic anisotropy of $CrPS_4$ (Supplementary Note 2). **f**, Evolution of H_{flop} for $H_\perp$, as a function of n_e. **g**, n_e-dependent interlayer exchange energy ratio J/J_0 (cyan diamonds for experimental data, orange diamonds for DFT calculations). J_0 is the interlayer exchange energy at the lowest doping, J_0^{DFT} ($n_e = 0$) = 1.1 meV for the DFT calculations, and J_0^{EXP} ($n_e = 1.75 \times 10^{11}$ cm^{-2}) = 0.58 meV for the experimental values (a trend towards flattening seen in the DFT calculations at large n_e remains to be understood). **h**, Uniaxial magnetic anisotropy K extracted from H_{flip} measured for both $H_\perp$ and $H_\parallel$ (see Supplementary Note 2 for details). The error bars in **e** and **f** are estimated from the width of the maximum/minimum in d^2G/dH^2 used to determine H_{flop} and H_{flip} (the width is taken at a 1% deviation from the maximum/minimum; see Supplementary Fig. 3 for an example). The error bars in **g** and **h** are calculated by propagating the errors shown in **e**.

field D/ε_0 and small accumulated electron density n_e (Fig. 1a). A large D/ε_0 maximizes the interlayer potential difference, responsible for the energy difference between opposite spin bands. A small n_e allows populating states with only one spin direction and ensures that the accumulated electrons do not affect the magnetic state[38].

Before exploring this regime, we characterize the devices at zero displacement field. The magnetoconductance $\delta G(H) = (G(H) - G_0)/G_0$ ($G(H)$ is the conductance measured at magnetic field $\mu_0 H$, and $G_0 = G(H = 0)$) of a $CrPS_4$ double-gated FET measured at zero displacement field is shown in Fig. 2, with magnetic field applied either perpendicular (out of plane; Fig. 2a,b) or parallel (in plane; Fig. 2c,d) to the layers. At low n_e, the spin-flip field (H_{flip}) is approximately 3.5 T (the field at which the magnetoconductance starts to flatten), half the bulk value, because each constituent layer feels the exchange interaction of only one neighbouring layer[43,44]. The precise value is determined by the minimum in d^2G/dH^2 (Supplementary Figs. 2 and 3), from which we see that H_{flip} decreases pronouncedly upon increasing n_e, and that H_{flip} is larger when the field is applied in-plane (see Fig. 2e and Supplementary Fig. 2 for details). The flat magnetoconductance observed at low magnetic field (Fig. 2b) also allows determining the spin-flop field H_{flop}[38,43] (Fig. 2f).

From these measurements, we extract quantitative values for the parameters determining the magnetic state of the $CrPS_4$ bilayer, the interlayer exchange energy J and the uniaxial magnetic anisotropy K (Methods and Supplementary Note 2). To this end, we express the magnetic energy of the system as $E = J\mathbf{M}_1 \cdot \mathbf{M}_2/M_s^2 - K/2\,(M_{1z}/M_s)^2 - K/2\,(M_{2z}/M_s)^2 - \mu_0\,\mathbf{H} \cdot (\mathbf{M}_1 + \mathbf{M}_2)$, where $\mathbf{M}_1$ and $\mathbf{M}_2$ are the magnetizations of the two layers owing to the Cr atoms, M_s is the single-layer saturation magnetization (per unit cell) and $\mathbf{H}$ is the applied magnetic field. The analysis of the spin-flip transition with in- and out-of-plane field (Fig. 2e) gives the values of J and K shown in Fig. 2g,h, both decreasing upon increasing n_e. Surprisingly, the magnetic anisotropy vanishes at $n_e > 7$–8×10^{12} cm^{-2} (K likely changes sign and the magnetization reorients to be in the plane[45], but under these conditions, our magnetoconductance measurements cannot be used to determine its value). The observed trends agree with ab initio calculations (Fig. 2g). The suppression of J can be understood as due to the already established downshift of the conduction band edge in the ferromagnetic state[39]. Because of this downshift, accumulating electrons increases the energy of the antiferromagnetic state (E_{AFM}) more than that of the ferromagnetic one (E_{FM}) so that the interlayer exchange energy J (related to $E_{FM}(n_e) - E_{AFM}(n_e)$) decreases.

We conclude that—when probing the existence of spin-polarized bands in the $CrPS_4$ bilayer—the charge density needs to be limited to values well below 7×10^{12} cm^{-2}, to avoid that the magnetic state of $CrPS_4$ is strongly affected by the accumulated electrons. We also conclude that the influence of the accumulated electrons on the magnetic state is well described by a large change in the values of J and K, and not in the magnetization of the layer where electrons are accumulated. Indeed, as n_e is increased up to approximately 10^{13} cm^{-2}, J changes by a factor of 2 and K vanishes, whereas the change in layer magnetization is smaller than 0.5% (the electron density is only approximately 1% of the density of Cr atoms and the spin of Cr is 3/2). We should therefore analyse the system by considering first that electrons populate states in the conduction band associated with the underlying magnetic structure created by the Cr atoms (determined considering that J and K are functions of n_e), and only later consider the effect of the modified layer magnetization.

Hysteretic magneto-transport

In the presence of a perpendicular displacement field and sufficiently low n_e, electrons are accumulated in the bottom or top layer depending on the sign of D. They occupy one of the spin-split bands, whose spin

https://doi.org/10.1038/s41565-025-01872-w

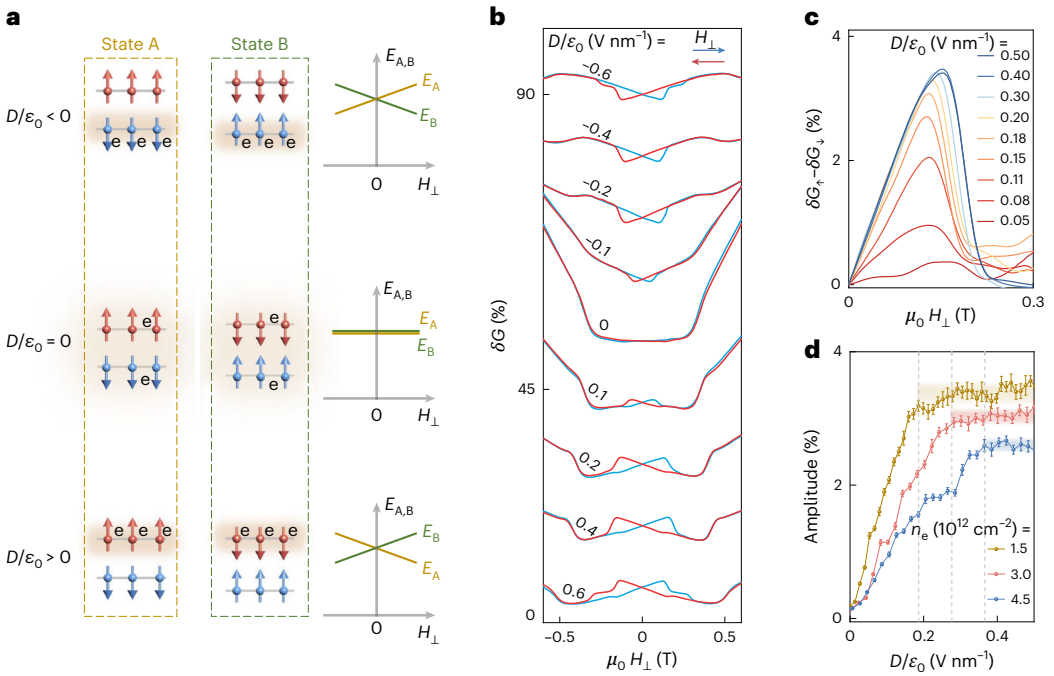

Fig. 3 | Detecting switchable spin-polarized bands in 2L $CrPS_4$. a, At small magnetic field, 2L $CrPS_4$ can be in one of the two states—with opposite magnetization in the top and bottom layers—labelled as A (left column) and B (right column). These states are energetically degenerate ($E_A = E_B$) in the absence of gate-induced electrons ($n_e = 0$) or when electrons equally occupy both layers ($D/\varepsilon_0 = 0$). The degeneracy is broken at finite n_e and perpendicular electric field D/ε_0, in the presence of a perpendicular magnetic field. The state with lower energy is determined by the sign of the applied electric and magnetic fields, because the energy difference arises from the Zeeman energy of accumulated electrons that—a low n_e—occupy states in one of the two layers (and are therefore spin-polarized with spin pointing in opposite directions; Fig. 1a). **b**, δG measured at different D/ε_0 (legend) at $n_e = 1.5 \times 10^{12}$ cm^{-2}. At $D/\varepsilon_0 = 0$, no hysteresis is observed owing to the degeneracy of states A and B, as expected. The hysteresis that appears at finite D/ε_0 when sweeping $H_\perp$ up or down provides direct experimental evidence for the existence of the two states with different energies in a finite perpendicular magnetic field. **c**, Magnetoconductance hysteresis, corresponding to the difference between the magnetoconductance measured with field swept up ($\delta G_\uparrow$) or down ($\delta G_\downarrow$) for different values of D/ε_0 (legend) and constant density $n_e = 1.5 \times 10^{12}$ cm^{-2}. The hysteresis amplitude first increases with D/ε_0 and then saturates. **d**, Hysteresis amplitude as a function of D/ε_0 for different carrier densities. The saturation threshold of D_{sat}/ε_0 shifts to higher values as the carrier density increases, as indicated by the dashed lines and shaded regions. The error bars in **d** are estimated from the noise level of the curves in **c**.

polarization is determined by the magnetization of the Cr atoms in the same layer (Fig. 1a). The system has then two possible states (labelled A and B) with opposite spin of the accumulated electrons (Fig. 3a). The two states are energetically degenerate at zero applied perpendicular magnetic field $H_\perp$, and their energies shift in opposite direction when sweeping $H_\perp$ towards positive or negative values, owing to the Zeeman energy of accumulated electrons. Even if the system is initialized in the low-energy state, therefore, it will eventually occupy the high-energy metastable state when the magnetic field is swept and changes sign. More specifically, when the magnetic field is swept from large negative values through the (negative) spin-flop field[46], there is no preference between states A and B if $D/\varepsilon_0 = 0$. With a finite D, however, the system develops a preference and favours the state with lower energy (as shown in Fig. 3a). As the magnetic field is swept to positive values, the system switches to the other state, resulting in an antiparallel magnetization arrangement, but with the Néel vector reversed (see Extended Data Fig. 3 for details). We then expect the magnetoconductance to be hysteretic if the two states with opposite electron magnetization exhibit different conductance.

Figure 3b shows the low-field magnetoconductance measured in a perpendicular magnetic field, at $n_e = 1.5 \times 10^{12}$ cm^{-2}, for different values of D/ε_0. Hysteresis emerges at finite D/ε_0, so that the magnetoconductance differs depending on whether the applied magnetic field is swept from negative to positive (blue curves) or from positive to negative (red curves) values. The hysteresis ends with a sharp jump at approximately $\mu_0 H = 0.2$ T, exhibiting a phenomenology typical of easy axis ferromagnets[47]. No hysteresis is observed for parallel magnetic field, as expected, since in a parallel field states A and B always have the same energy (see Extended Data Fig. 4 for details). The observed behaviour therefore confirms that electrons generate a net magnetization as they populate the spin-split conduction band of the $CrPS_4$ bilayer, owing to the symmetry breaking induced by the applied displacement field (virtually identical behaviour has been seen in another double-gated device; Supplementary Fig. 4). The switching between the two magnetic states may occur with the bilayer staying in a single domain (as in the Stoner–Wohlfarth model[47]) or by breaking the $CrPS_4$ bilayers into magnetic domains[47]. In the latter case, reversing the magnetic field sweep direction halfway the hysteresis loop should result in 'minority' hysteresis loops, with the magnetoconductance that does not re-trace the curve measured when the magnetic field is swept up to $H > H_{flop}$. This is indeed what we observe experimentally (Supplementary Fig. 5).

Figure 3c shows how the magnitude of the magnetoconductance hysteresis evolves upon increasing displacement field D/ε_0, with data measured at a fixed carrier density $n_e = 1.5 \times 10^{12}$ cm^{-2}. Starting from $D/\varepsilon_0 = 0$, $\delta G_\uparrow - \delta G_\downarrow$ first increases rapidly, before saturating at approximately $D/\varepsilon_0 = 0.18$ V nm^{-1}. The dependence of the magnitude (quantified by the peak value of $\delta G_\uparrow - \delta G_\downarrow$) is summarized by the brown dots in Fig. 3d. Measurements at larger values of accumulated electron density n_e exhibit the overall same behaviour (red and blue dots in Fig. 3d), but the displacement field needed to reach saturation increases. The trend is consistent with the behaviour expected for a conduction band spin-splitting induced by the displacement field (as shown in Fig. 1a). As D/ε_0 is initially turned on, the spin-splitting is small—much smaller than the Fermi energy corresponding to the accumulated charge density—so that both the spin-up and spin-down bands in the two layers

https://doi.org/10.1038/s41565-025-01872-w

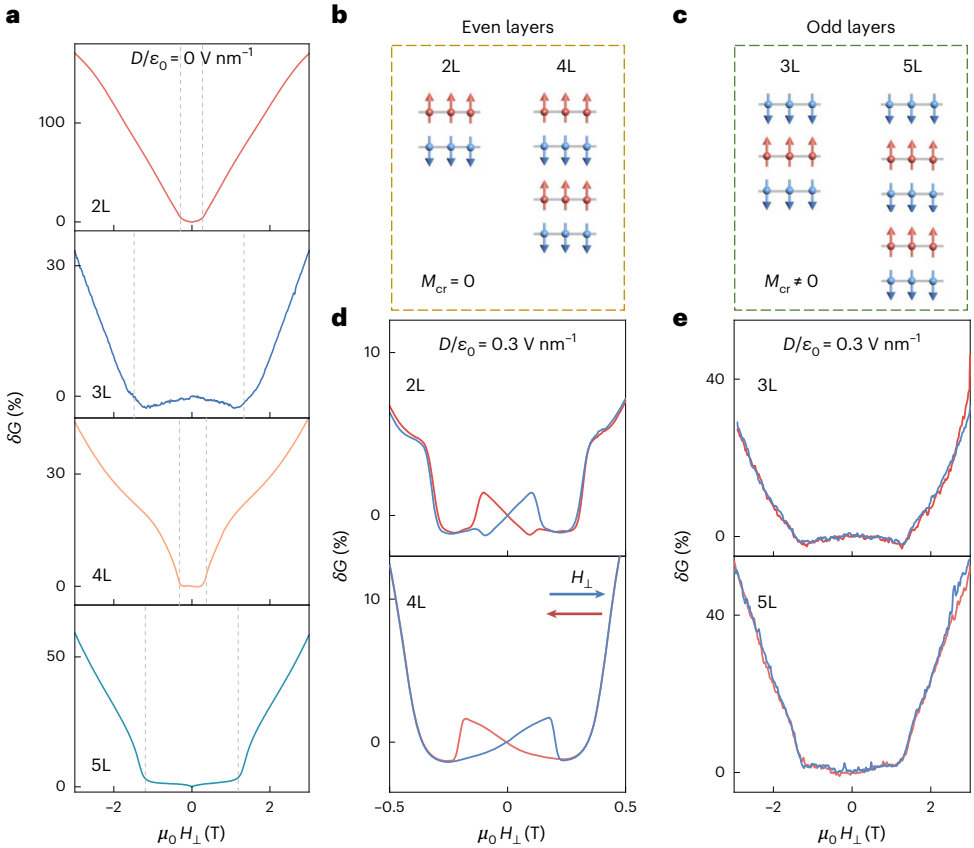

Fig. 4 | Odd–even effect of magnetoconductance hysteresis. **a**, Magnetoconductance $\delta G(H)$ measured at 2 K and zero electric field ($D/\varepsilon_0 = 0$, $n_e \approx 4.5 \times 10^{12}$ cm^{-2}) on double-gated devices based on 2L, 3L, 4L and 5L $CrPS_4$ (from top to bottom, see legends). The spin-flop transition (indicated by the dashed lines) in odd layers occurs at 2–3 times larger field than in even layers (approximately 0.5 T), as expected for weakly anisotropic layered antiferromagnets[43,49]. In the absence of an applied displacement field, no magnetoresistance hysteresis is observed irrespective of layer thickness. **b**, Schematic representation of the A-type magnetic order in even number of CrS_4 layers, where red (blue) arrows represent the magnetization of the Cr atoms in each layer. For even layers, the total magnetization owing to the Cr atoms vanishes. **c**, Same as in **b** but for odd number of CrS_4 layers. The total magnetization of Cr atoms is finite owing to the presence of an unpaired layer. **d**, Magnetoconductance $\delta G(H)$ measured at 2 K on even layers (2L and 4L) at $D/\varepsilon_0 = 0.3$ V nm^{-1} and $n_e \approx 4.5 \times 10^{12}$ cm^{-2}, exhibiting a clear hysteresis when sweeping the perpendicular magnetic field ($H_\perp$). **e**, Magnetoconductance δG (H, 2 K) measured on odd layers (3L and 5L) at $D/\varepsilon_0 = 0.3$ V nm^{-1} and $n_e \approx 4.5 \times 10^{12}$ cm^{-2}, exhibiting no hysteresis below spin-flop field even when an applied perpendicular displacement field is present.

are populated. The population of the two bands is only slightly different, which is why the amplitude of the hysteresis is small. As D/ε_0 is increased, the spin-splitting in the conduction band also increases, and so does the difference in population of spin-up and -down bands, which is why the amplitude of $\delta G_\uparrow - \delta G_\downarrow$ also increases. At sufficiently large D/ε_0, the splitting between the spin-up and -down bands becomes larger than the Fermi energy, so that the electrons populate only one of the bands. Past this point, a further increase in D/ε_0 does not change the population of the spin-split bands, and $\delta G_\uparrow - \delta G_\downarrow$ saturates.

This scenario naturally explains why the accumulation of a larger electron density n_e requires a larger displacement field to reach saturation. We estimate the value of displacement field at saturation as $D_{sat}/\varepsilon_0 = n_e \varepsilon_r/(e\, d\, (m^*/2\pi\hbar^2))$ by equating the induced electrostatic energy difference between the two layers to the Fermi energy of the electrons occupying one layer (d is the distance between the $CrPS_4$ layers forming the bilayer, ε_r is the relative dielectric constant (3.9), m^* is the effective mass (1.26 times the free electron mass) in $CrPS_4$ (ref. 48), e is the electron charge, and $\hbar$ is Planck's constant). For $n_e = 1.5 \times 10^{12}$ cm^{-2}, $D_{sat}/\varepsilon_0 \approx 0.3$ V nm^{-1}, close to the experimental value. Both the argument invoked to explain the evolution of the magnetoconductance hysteresis with displacement field and the good correspondence between the estimated and measured values of D_{sat}/ε_0 support the scenario that the conduction band is fully spin-polarized for $D/\varepsilon_0 > D_{sat}/\varepsilon_0$.

Odd–even effects

To confirm that a vertical displacement field causes a hysteretic magnetoconductance because of the effect of inversion symmetry breaking on the accumulated electrons, we have explored devices realized on 3, 4 and 5 $CrPS_4$ layers (3L, 4L and 5L; Fig. 4). Even (2L and 4L) and odd (3L and 5L) $CrPS_4$ multilayers should exhibit distinctly different behaviour, because in odd layers the magnetization of the top and bottom layers is the same, whereas in even layers it is opposite. Reversing the displacement field polarity, therefore, alters the spin polarization of gate-accumulated electrons only in even layers. In addition, in odd multilayers, the magnetization of the uncompensated layer of Cr atoms ($M_{Cr} \neq 0$) is nearly thousand times larger than that of the accumulated electrons. Therefore, in odd multilayers, the magnetization is large already in the absence of any accumulated electron and switches at small applied magnetic field (around 0.05 T)[37]. In other words, in odd layers, the switching between state A and state B (see schematics in Fig. 3 for bilayers) is driven by the uncompensated layer's magnetization: since the conductance does not depend on whether the Cr magnetization points up or down, the switch between states A and B in odd layers has no measurable effect on transport.

Figure 4 shows magnetoconductance data for 3–5L $CrPS_4$. At $D/\varepsilon_0 = 0$, no hysteresis is observed below the spin-flop field irrespective of layer thickness, as expected. A very pronounced odd–even

https://doi.org/10.1038/s41565-025-01872-w

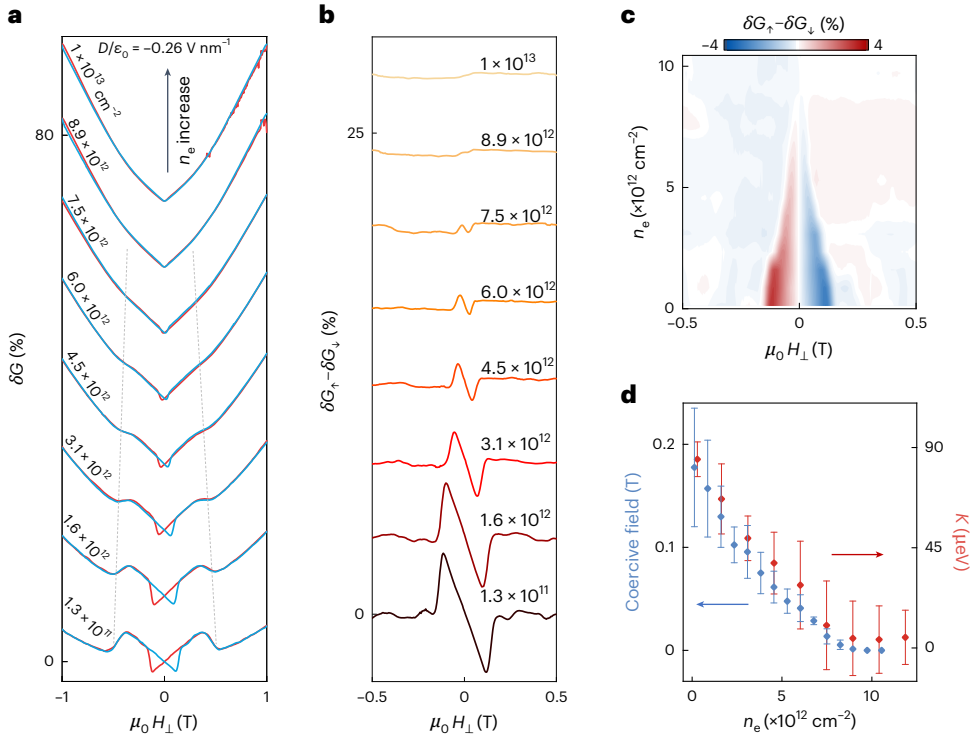

Fig. 5 | Dependence of the magnetic state on electron density. a, Low-field magnetoconductance $\delta G(H_\perp)$ measured for increasing values of accumulated electron density n_e (legend), at constant $D/\varepsilon_0 = -0.26$ V nm^{-1} (see Supplementary Fig. 7 for analogous data at positive D/ε_0). The hysteresis caused by the finite magnetization of electrons occupying spin-polarized bands becomes less pronounced—and the magnetic field at which the hysteresis ends (that is, the coercive field) becomes smaller—upon increasing n_e. Both quantities eventually vanish at approximately 7–8 × 10^{12} cm^{-2}. The feature associated to the spin-flop transition (indicated by the grey dashed lines) also shifts to lower magnetic fields, becomes less pronounced and eventually disappears on the same n_e scale. **b**,**c**, Amplitude of the magnetoconductance hysteresis ($\delta G_\uparrow - \delta G_\downarrow$) obtained from **a** for different values of n_e (**b**) and colour plot of $\delta G_\uparrow - \delta G_\downarrow$ as a function of n_e and $H_\perp$ (**c**), both showing that the hysteresis vanishes at $n_e \approx 7$–8 × 10^{12} cm^{-2}. **d**, The carrier density evolution of the coercive field extracted from **b** and **c**, and of the uniaxial magnetic anisotropy K extracted from the analysis of the spin-flip field in parallel and perpendicular magnetic field, shows that the two quantities are proportional. The error bars for the coercive field correspond to the width of the jump shown in **b**. K and its error bars are extracted using the same method used to extract the data shown in Fig. 2e.

effect is evident in the spin-flop transition fields, with even layers transitioning at approximately 0.5 T and odd layers at 2–3 times larger field (Fig. 4a). This difference originates from the magnetization of the uncompensated layer present in odd multilayers (Fig. 4b,c), which shifts the spin-flop transition to higher magnetic field (see earlier work on CrSBr and $CrCl_3$)[43,49]. More importantly, when an electric field is applied, the behaviour of even and odd layers becomes markedly different. Hysteresis in the magnetoconductance emerges, but only in even layers (Fig. 4d): odd layers continue to show no hysteresis (Fig. 4e). The amplitude of the magnetoconductance hysteresis in 4L $CrPS_4$ is comparable to that of 2L $CrPS_4$, even though detailed aspects are different. For instance, increasing the displacement field from a negative (−0.6 V nm^{-1}) to a positive value (0.6 V nm^{-1}) causes the sign of the magnetoconductance hysteresis in 4L to change multiple times (Supplementary Fig. 6). This is likely because the electronic wavefunctions evolve from being distributed equally over all layers at $D/\varepsilon_0 = 0$ to be localized only on the outer layer (top or bottom depending on the sign of D), causing multiple changes in the electronic magnetization. Irrespective of these details, the key conclusion is that the magnetoconductance hysteresis is observed only in even $CrPS_4$ multilayers, owing to inversion symmetry caused by a finite displacement field.

Doping-dependent hysteresis

Finally, we discuss the evolution of the magnetoconductance hysteresis in bilayers as the carrier density is increased past the value at which the uniaxial magnetic anisotropy K vanishes. If the sign of K changes, as we expect for $n_e > 7$–8 × 10^{12} cm^{-2}, the magnetization in 2L $CrPS_4$ reorients to point in-plane. States A and B then have the same energy at a finite magnetic field, and no switching—hence no magnetoconductance hysteresis—should be observed. This is what we find if we measure the magnetoconductance at a fixed D ($D/\varepsilon_0 = -0.26$ V nm^{-1} in Fig. 5a) for increasing values of n_e: the hysteresis becomes less pronounced, the coercive field decreases, and vanishes around $n_e \approx 7$–8 × 10^{12} cm^{-2}. Figure 5b,c summarizes the evolution of the hysteretic part of the magnetoconductance ($\delta G_\uparrow - \delta G_\downarrow$). Figure 5d shows that the coercive field extracted from this data scales with n_e as the uniaxial magnetic anisotropy constant (Fig. 2h). Consistently, we also see that the spin-flop transition—proportional to $\sqrt{K}$—shifts to lower magnetic fields, becomes less pronounced and eventually vanishes (Fig. 5a). Similar trends are observed for 4L $CrPS_4$ (Supplementary Fig. 6).

Conclusion

The switchable magneto-transport hysteresis reported here shows directly the relation between spatial symmetry breaking—inversion symmetry in the present case—and the existence of spin-polarized bands in antiferromagnets. Controlling spatial symmetries using FETs based on 2D antiferromagnetic semiconductors introduces new functionalities, possibly relevant for antiferromagnetic spintronics, such as the ability to switch on and off spin-dependent transport at will, in principle at high frequency. Furthermore, double-gated $CrPS_4$ bilayers provide a very promising platform to realize gate-induced conductors with near unity spin polarization[50], that is, transistors in which not only the flow of charge but also the flow of spin is controlled. The evolution

of the amplitude of hysteretic magnetoconductance with displacement field (Fig. 3d) strongly suggests that at a sufficiently large D and low electron density, only one spin-polarized band is occupied, implying that in double-gate $CrPS_4$ bilayer transistors, the dominant spin of the electrons responsible for charge transport can be controllably switched by gate. Conceiving feasible experiments to validate this conclusion—that is, to directly measure the spin polarization of the accumulated electrons as a function of displacement field—is a key milestone for upcoming work.

Finally, when the mobility of charge carriers will be improved, we expect double-gated transistors of $CrPS_4$ bilayers to give control over the sign of anomalous Hall effect. At zero perpendicular electric displacement field—in the absence of spin polarization—no anomalous Hall effect should be observed. As the displacement field is turned on, the anomalous Hall effect should emerge with a sign determined by the sign of D, which fixes the sign of the spin polarization. Gate switchable spin polarization and anomalous Hall effect have never been investigated earlier in bilayer antiferromagnets, and we expect that improving the material quality may allow exploring these phenomena and discovering others.

Online content

Any methods, additional references, Nature Portfolio reporting summaries, source data, extended data, supplementary information, acknowledgements, peer review information; details of author contributions and competing interests; and statements of data and code availability are available at https://doi.org/10.1038/s41565-025-01872-w.

References

1. Chen, H., Niu, Q. & MacDonald, A. H. Anomalous Hall effect arising from noncollinear antiferromagnetism. *Phys. Rev. Lett.* **112**, 017205 (2014).
2. Smejkal, L., Gonzalez-Hernandez, R., Jungwirth, T. & Sinova, J. Crystal time-reversal symmetry breaking and spontaneous Hall effect in collinear antiferromagnets. *Sci. Adv.* **6**, eaaz8809 (2020).
3. Mazin, I. Altermagnetism—a new punch line of fundamental magnetism. *Phys. Rev. X* **12**, 040002 (2022).
4. Šmejkal, L., Sinova, J. & Jungwirth, T. Emerging research landscape of altermagnetism. *Phys. Rev. X* **12**, 040501 (2022).
5. Yan, H., Zhou, X., Qin, P. & Liu, Z. Review on spin-split antiferromagnetic spintronics. *Appl. Phys. Lett.* **124**, 030503 (2024).
6. Sinova, J. et al. Spin Hall effects. *Rev. Mod. Phys.* **87**, 1213–1260 (2015).
7. Jungwirth, T., Marti, X., Wadley, P. & Wunderlich, J. Antiferromagnetic spintronics. *Nat. Nanotechnol.* **11**, 231–241 (2016).
8. Baltz, V. et al. Antiferromagnetic spintronics. *Rev. Mod. Phys.* **90**, 015005 (2018).
9. Šmejkal, L., Mokrousov, Y., Yan, B. & MacDonald, A. H. Topological antiferromagnetic spintronics. *Nat. Phys.* **14**, 242–251 (2018).
10. Nakatsuji, S., Kiyohara, N. & Higo, T. Large anomalous Hall effect in a non-collinear antiferromagnet at room temperature. *Nature* **527**, 212–215 (2015).
11. Gao, A. et al. Layer Hall effect in a 2D topological axion antiferromagnet. *Nature* **595**, 521–525 (2021).
12. Šmejkal, L. et al. Anomalous Hall antiferromagnets. *Nat. Rev. Mater.* **7**, 482–496 (2022).
13. Feng, Z. et al. An anomalous Hall effect in altermagnetic ruthenium dioxide. *Nat. Electron.* **5**, 735–743 (2022).
14. Železný, J., Zhang, Y., Felser, C. & Yan, B. Spin-polarized current in noncollinear antiferromagnets. *Phys. Rev. Lett.* **119**, 187204 (2017).
15. Yuan, L.-D. et al. Giant momentum-dependent spin splitting in centrosymmetric low-Z antiferromagnets. *Phys. Rev. B* **102**, 014422 (2020).
16. Zhu, Y.-P. et al. Observation of plaid-like spin splitting in a noncoplanar antiferromagnet. *Nature* **626**, 523–528 (2024).
17. Krempaský, J. et al. Altermagnetic lifting of Kramers spin degeneracy. *Nature* **626**, 517–522 (2024).
18. Gibertini, M., Koperski, M., Morpurgo, A. F. & Novoselov, K. S. Magnetic 2D materials and heterostructures. *Nat. Nanotechnol.* **14**, 408–419 (2019).
19. Gong, C. & Zhang, X. Two-dimensional magnetic crystals and emergent heterostructure devices. *Science* **363**, eaav4450 (2019).
20. Mak, K. F., Shan, J. & Ralph, D. C. Probing and controlling magnetic states in 2D layered magnetic materials. *Nat. Rev. Phys.* **1**, 646–661 (2019).
21. Huang, B. et al. Emergent phenomena and proximity effects in two-dimensional magnets and heterostructures. *Nat. Mater.* **19**, 1276–1289 (2020).
22. Sierra, J. F. et al. Van der Waals heterostructures for spintronics and opto-spintronics. *Nat. Nanotechnol.* **16**, 856–868 (2021).
23. Kurebayashi, H. et al. Magnetism, symmetry and spin transport in van der Waals layered systems. *Nat. Rev. Phys.* **4**, 150–166 (2022).
24. Gong, S. J. et al. Electrically induced 2D half-metallic antiferromagnets and spin field effect transistors. *Proc. Natl Acad. Sci. USA* **115**, 8511–8516 (2018).
25. Lv, H., Niu, Y., Wu, X. & Yang, J. Electric-field tunable magnetism in van der Waals bilayers with A-type antiferromagnetic order: unipolar versus bipolar magnetic semiconductor. *Nano Lett.* **21**, 7050–7055 (2021).
26. Deng, J. et al. Two-dimensional bipolar ferromagnetic semiconductors from layered antiferromagnets. *Phys. Rev. Mater.* **5**, 034005 (2021).
27. Dang, W. et al. Electric-field-tunable spin polarization and carrier-transport anisotropy in an A-type antiferromagnetic van der Waals bilayer. *Phys. Rev. Appl.* **18**, 064086 (2022).
28. Marian, D. et al. Electrically tunable lateral spin-valve transistor based on bilayer CrI_3. *npj 2D Mater. Appl.* **7**, 42 (2023).
29. Oostinga, J. B. et al. Gate-induced insulating state in bilayer graphene devices. *Nat. Mater.* **7**, 151–157 (2008).
30. Zhang, Y. et al. Direct observation of a widely tunable bandgap in bilayer graphene. *Nature* **459**, 820–823 (2009).
31. Huang, B. et al. Electrical control of 2D magnetism in bilayer CrI_3. *Nat. Nanotechnol.* **13**, 544–548 (2018).
32. Jiang, S. et al. Controlling magnetism in 2D CrI_3 by electrostatic doping. *Nat. Nanotechnol.* **13**, 549–553 (2018).
33. Jiang, S., Shan, J. & Mak, K. F. Electric-field switching of two-dimensional van der Waals magnets. *Nat. Mater.* **17**, 406–410 (2018).
34. Lee, J. et al. Structural and optical properties of single- and few-layer magnetic semiconductor $CrPS_4$. *ACS Nano* **11**, 10935–10944 (2017).
35. Calder, S. et al. Magnetic structure and exchange interactions in the layered semiconductor $CrPS_4$. *Phys. Rev. B* **102**, 024408 (2020).
36. Peng, Y. et al. Magnetic structure and metamagnetic transitions in the van der Waals antiferromagnet $CrPS_4$. *Adv. Mater.* **32**, 2001200 (2020).
37. Son, J. et al. Air-stable and layer-dependent ferromagnetism in atomically thin van der Waals $CrPS_4$. *ACS Nano* **15**, 16904–16912 (2021).
38. Wu, F. et al. Gate-controlled magnetotransport and electrostatic modulation of magnetism in 2D magnetic semiconductor $CrPS_4$. *Adv. Mater.* **35**, e2211653 (2023).
39. Wu, F. et al. Magnetism-induced band-edge shift as the mechanism for magnetoconductance in $CrPS_4$ transistors. *Nano Lett.* **23**, 8140–8145 (2023).

40. Wang, Z. et al. Very large tunneling magnetoresistance in layered magnetic semiconductor CrI_3. *Nat. Commun.* **9**, 2516 (2018).
41. Li, J., Gutierrez-Lezama, I. & Morpurgo, A. F. Magneto-transport study in 2D magnetic semiconductor multi-terminal FET. *Zenodo* https://doi.org/10.5281/zenodo.12702065 (2024).
42. Chang, J.-F. et al. Hall-effect measurements probing the degree of charge-carrier delocalization in solution-processed crystalline molecular semiconductors. *Phys. Rev. Lett.* **107**, 066601 (2011).
43. Wang, Z. et al. Determining the phase diagram of atomically thin layered antiferromagnet $CrCl_3$. *Nat. Nanotechnol.* **14**, 1116–1122 (2019).
44. Yao, F. et al. Multiple antiferromagnetic phases and magnetic anisotropy in exfoliated $CrBr_3$ multilayers. *Nat. Commun.* **14**, 4969 (2023).
45. Tang, M. et al. Continuous manipulation of magnetic anisotropy in a van der Waals ferromagnet via electrical gating. *Nat. Electron.* **6**, 28–36 (2023).
46. Clark, A. E. & Callen, E. Néel ferrimagnets in large magnetic fields. *J. Appl. Phys.* **39**, 5972–5982 (1968).
47. Coey, J. M. *Magnetism and Magnetic Materials* (Cambridge Univ. Press, 2010).
48. Zhuang, H. L. & Zhou, J. Density functional theory study of bulk and single-layer magnetic semiconductor $CrPS_4$. *Phys. Rev. B* **94**, 195307 (2016).
49. Ye, C. et al. Layer-dependent interlayer antiferromagnetic spin reorientation in air-stable semiconductor CrSBr. *ACS Nano* **16**, 11876–11883 (2022).
50. Son, Y.-W., Cohen, M. L. & Louie, S. G. Half-metallic graphene nanoribbons. *Nature* **444**, 347–349 (2006).

Methods

Device fabrication

The h-BN/$CrPS_4$/graphite (Gr)/h-BN heterostructures were assembled using a dry pick-up and transfer technique with PDMS-PC stamps in an N_2-filled glove box (H_2O <0.1 ppm, O_2 <0.1 ppm). $CrPS_4$ multilayers were obtained via micromechanical exfoliation inside the glove box from bulk crystals purchased from HQ Graphene. The chemical composition and stoichiometry of $CrPS_4$ bulk crystals were verified using energy-dispersive X-ray spectroscopy in a scanning electron microscope, with elemental mapping showing a uniform distribution and an atomic ratio of Cr:P:S as 16.92:16.60:66.48, consistent with the expected 1:1:4 stoichiometry[38]. Graphene and h-BN flakes were prepared by mechanical exfoliation onto SiO_2/Si substrates. The $CrPS_4$ crystals were encapsulated with top and bottom h-BN layers. Separate graphite stripes acted as source–drain electrodes and were connected to metallic pads via edge contacts located far from the $CrPS_4$ crystal. The edge contacts and metallic pads were fabricated using electron-beam lithography, reactive-ion etching, electron-beam evaporation of 10 nm Cr followed by 50 nm Au, and a lift-off process. Cr/Au contact electrodes were also deposited on the top h-BN to form the top gate. As the bottom gate electrode, we used the highly doped Si substrate, with the SiO_2 layer serving as gate dielectric together with the bottom h-BN crystal. In total, we fabricated nine devices using thin $CrPS_4$ layers. We fabricated one device each for 2L, 3L and 4L in a single-gate configuration, with only the bilayer and four-layer devices exhibiting hysteresis. To study the independent effects of the electric field and doping, we fabricated two 2L devices, two 4L devices, one 3L device and one 5L device in a double-gate configuration. The thickness of $CrPS_4$ was determined using optical contrast and Raman spectroscopy (see Extended Data Fig. 2 for details).

Transport measurement

Low-noise homemade electronics in combination with commercial electronics was used to bias the top and bottom gate electrodes, to apply source–drain voltage and to measure the current. Top-gate voltage (V_{TG}) and bottom-gate voltage (V_{BG}) were swept to adjust the doping density ($n_e = [C_t (V_{TG} - V_{TGTH}) + C_b (V_{BG} - V_{BGTH})]/e$) and the electric displacement field ($D/\varepsilon_0 = [(V_{TG} - V_{TGTH})/d_t - (V_{BG} - V_{BGTH})/d_b]/2$). C_t and C_b are top- and bottom-gate capacitance per unit area; V_{TGTH} and V_{BGTH} are threshold voltages when sweeping the back gate and top gate, respectively; d_t is the thickness of the top h-BN; d_b is the combined thickness of bottom h-BN and SiO_2 layers. Low-temperature transport measurements were conducted in an Oxford Instruments cryostat equipped with a superconducting magnet and a ^{3}He insert.

Antiferromagnetic two-site model

To model the energetics of the bilayer, we assume that the ferromagnetic intralayer exchange coupling is so strong (compared with the weak antiferromagnetic interlayer exchange coupling and the external magnetic field) that each layer can be considered as a single unit with uniform magnetization. Each layer thus behaves as a macroscopic spin that is coupled antiferromagnetically to its neighbour, so that the average magnetic energy per unit cell can be written as[43]

$$E = J\mathbf{M}_1 \cdot \mathbf{M}_2/M_S^2 - K/2(M_{1z}/M_S)^2 - K/2(M_{2z}/M_S)^2 - \mu_0 \mathbf{H} \cdot (\mathbf{M}_1 + \mathbf{M}_2),$$

where J is the antiferromagnetic interlayer exchange coupling, K is the magnetic anisotropy energy favouring out-of-plane orientation, $\mathbf{M}_1$ and $\mathbf{M}_2$ are the magnetization vectors of the two layers and $\mathbf{H}$ is the applied magnetic field. Here $M_s = 2g\mu_B S$ is the saturation magnetization (per unit cell) for a single layer, which can be easily computed from the nominal valence state of Cr atoms in $CrPS_4$ (corresponding to $S = 3/2$).

Density functional theory calculations

The total energy of the bilayer in the ferromagnetic and antiferromagnetic configurations has been computed from first principles using density functional theory (DFT) as implemented in Quantum ESPRESSO distribution[51,52]. Atomic positions for the bilayer have been extracted from the bulk relaxed crystal structure[38]. We have verified that, relaxing the atomic positions, the interlayer distance in the bilayer is only marginally changed with respect to the bulk material. The total energy is obtained adopting the Perdew–Burke–Ernzerhof exchange-correlation functional[53] with pseudopotentials taken from the Standard Solid-State Pseudopotential (SSSP) accuracy library (v1.0)[54] (cut-offs of ~40 Ry and ~320 Ry for wavefunctions and density). Hubbard corrections have not been included in the calculations. The interlayer exchange energy (per unit cell) is then evaluated as half the energy difference between the ferromagnetic and antiferromagnetic configurations, $J = (E_{FM} - E_{AFM})/2$. The 2D nature of the system is taken into account by using a Coulomb cut-off while the effect of doping is simulated using a double-gate field-effect set-up[55]. To sample the small Fermi surface at finite doping, a dense 24 × 24 × 1 Monkhorst–Pack grid over the Brillouin zone is adopted, with a Gaussian smearing of 6.4 meV.

Data availability

All relevant data are available from the corresponding authors upon request. Source data are provided with this paper.

Code availability

All codes adopted for DFT calculation are available from the corresponding authors upon request.

References

51. Giannozzi, P. et al. QUANTUM ESPRESSO: a modular and open-source software project for quantum simulations of materials. *J. Condens. Matter Phys.* **21**, 395502 (2009).
52. Giannozzi, P. et al. Advanced capabilities for materials modelling with Quantum ESPRESSO. *J. Condens. Matter Phys.* **29**, 465901 (2017).
53. Perdew, J. P., Burke, K. & Ernzerhof, M. Generalized gradient approximation made simple. *Phys. Rev. Lett.* **77**, 3865 (1996).
54. Prandini, G. et al. Precision and efficiency in solid-state pseudopotential calculations. *npj Comput. Mater.* **4**, 72 (2018).
55. Sohier, T., Calandra, M. & Mauri, F. Density functional perturbation theory for gated two-dimensional heterostructures: theoretical developments and application to flexural phonons in graphene. *Phys. Rev. B* **96**, 075448 (2017).

Acknowledgements

We gratefully acknowledge A. Ferreira for technical support and useful discussions with V. Multian, D. Lebedev and N. Ubrig. A.F.M. gratefully acknowledges the Swiss National Science Foundation (Division II, project #200020_178891) and the EU Graphene Flagship project for support. M.G. acknowledges support from Ministero Italiano dell'Università e della Ricerca through the PNRR project ECS_00000033_ECOSISTER and the PRIN2022 project SECSY. K.W. and T.T. acknowledge support from the JSPS KAKENHI (grant numbers 21H05233 and 23H02052) and World Premier International Research Center Initiative (WPI), MEXT, Japan.

Author contributions

F.Y., M.L. and A.F.M. initiated the work on atomically thin layers $CrPS_4$ field-effect transistors. F.Y. and M.L. fabricated the devices and performed the transport measurements with the assistance of I.G.-L., C.-Y.C., X.L. and F.W. M.G. performed the theoretical calculations. T.T. and K.W. grew and provided the h-BN crystals. F.Y., M.G., M.L., I.G.-L. and A.F.M. analysed the data and wrote the paper with input from all authors. I.G.-L. and A.F.M. supervised the research.

Funding

Open access funding provided by University of Geneva.

Competing interests
The authors declare no competing interests.

Additional information
Extended data is available for this paper at https://doi.org/10.1038/s41565-025-01872-w.

Supplementary information The online version contains supplementary material available at https://doi.org/10.1038/s41565-025-01872-w.

Correspondence and requests for materials should be addressed to Fengrui Yao, Marco Gibertini or Alberto F. Morpurgo.

Peer review information *Nature Nanotechnology* thanks the anonymous reviewers for their contribution to the peer review of this work.

https://doi.org/10.1038/s41565-025-01872-w

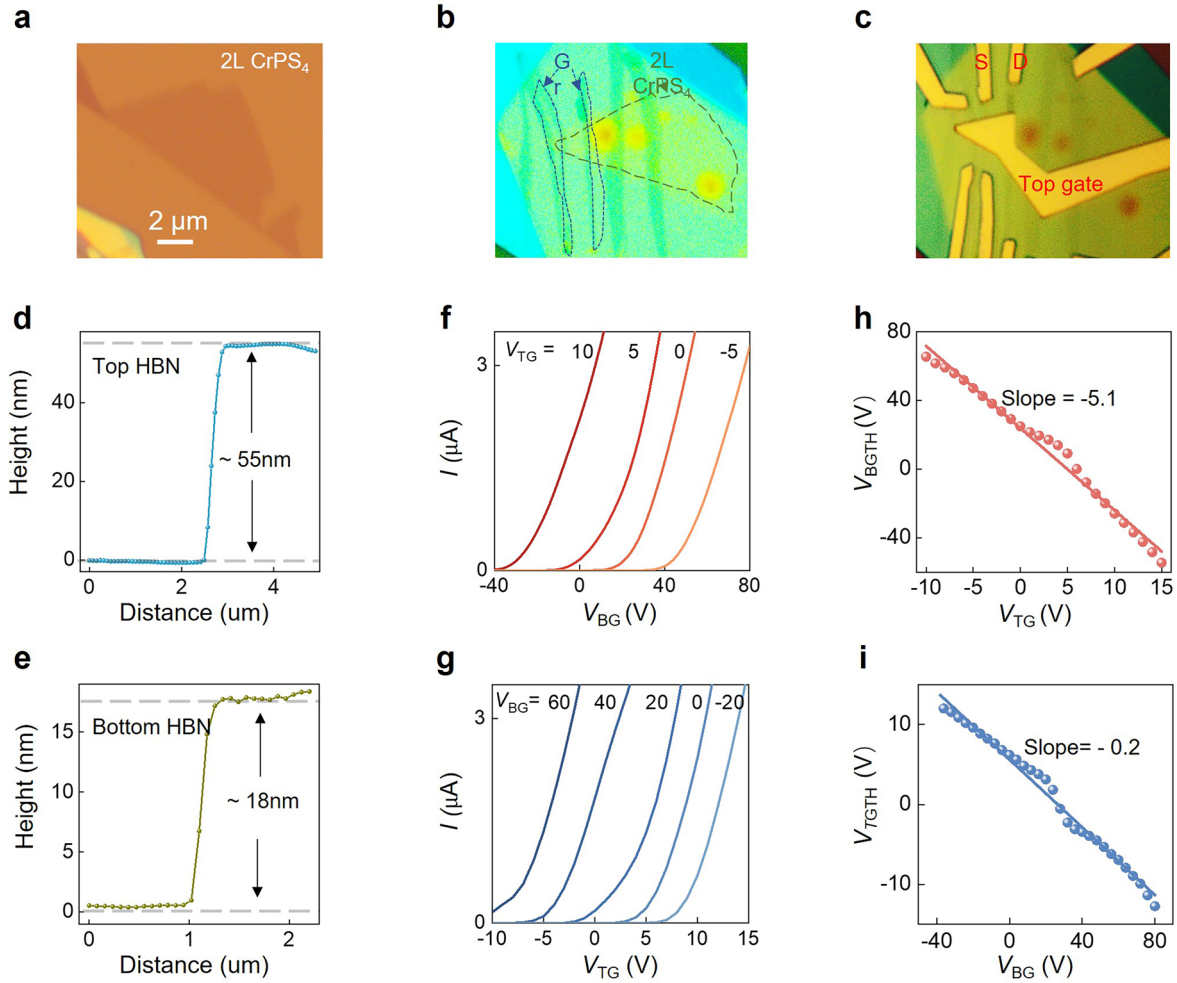

Extended Data Fig. 1 | Double-gated bilayer (2 L) $CrPS_4$ field effect transistor (FETs). a-c, Optical microscope images of the 2 L CrPS4 FET whose data is shown in the main text, at different stages of fabrication. **a**, Exfoliated 2 L $CrPS_4$ crystal on top of a 285 nm SiO2/Si substrate. **b**, h-BN/ $CrPS_4$ /graphite (Gr)/h-BN heterostructure assembled via a dry-pick up and transfer technique within the protective environment of a glovebox. The graphite stripes serve as electrodes for the transistor, and the top and bottom h-BN crystals encapsulate the 2 L $CrPS_4$ to protect it from the environment during subsequent fabrications steps outside the glovebox. **c**, Completed double-gated FET. Electron-beam lithography and evaporation are used to fabricate the Cr/Au metal layers serving as contacts to the Gr electrodes (edge contacts) and as top-gate electrode (top h-BN serves as top-gate dielectric). The bottom gate electrode is the highly doped Si substrate and the bottom gate dielectric is composed by the 285 nm SiO_2 layer together with the bottom h-BN crystal. **d-e**, Atomic force microscope height profile of the top and bottom h-BN crystals. **f, g**, Transfer curves measured at 2 K as a function of bottom (top) gate voltage V_{BG} (V_{TG}), while keeping the top (bottom) gate at a constant potential (at the values indicated in the figures). **h, i**, Back gate and top gate threshold voltage, V_{BGTH} and V_{TGTH}, plotted as a function of the potential applied to the opposite gate. The slope of V_{BGTH} vs V_{TG} in **f** and of V_{TGTH} vs V_{BG} in **g** are consistent with the corresponding ratios between the top and bottom gate capacitances. The threshold voltage values in **h** (**i**) are extracted by extrapolating the linear regime of the transfer curves shown in **f** (**g**) to zero current Source data.

https://doi.org/10.1038/s41565-025-01872-w

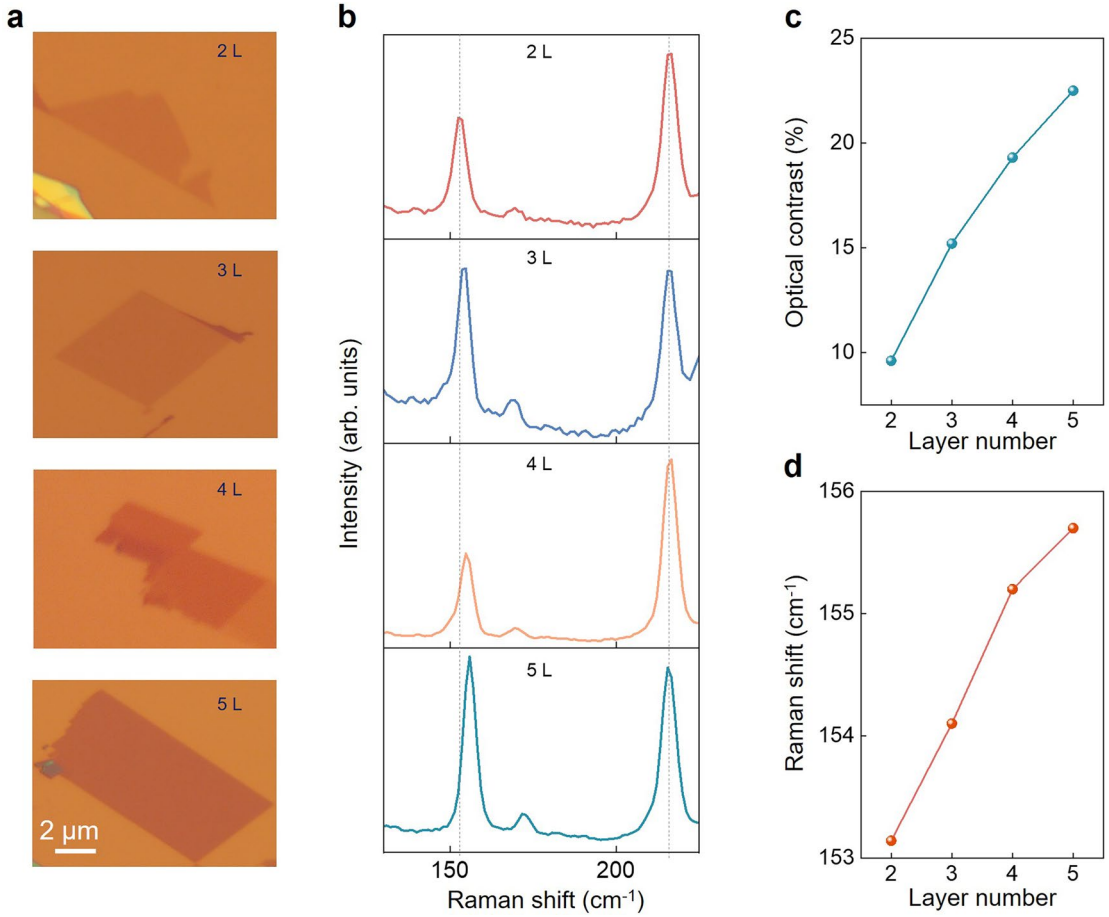

Extended Data Fig. 2 | Thickness characterization of atomically thin $CrPS_4$ multilayers. a, Optical micrographs of $CrPS_4$ multilayers with thicknesses ranging from 2 L to 5 L. **b**, Raman spectra of $CrPS_4$ multilayers, showing a redshift in the peak near 150 cm^{-1} as thickness increases, consistent with previously reported thickness-dependent shifts1, 2. **c**, Extracted optical contrast value of $CrPS_4$ multilayers with thicknesses from 2 L to 5 L. **d**, Extracted peak positions of the Raman mode around 150 cm^{-1} for multilayers with thicknesses from 2 L to 5 L. These results demonstrate that the layer number of thin $CrPS_4$ can be identified through the redshift in the Raman peak and corresponding changes in optical contrast Source data.

https://doi.org/10.1038/s41565-025-01872-w

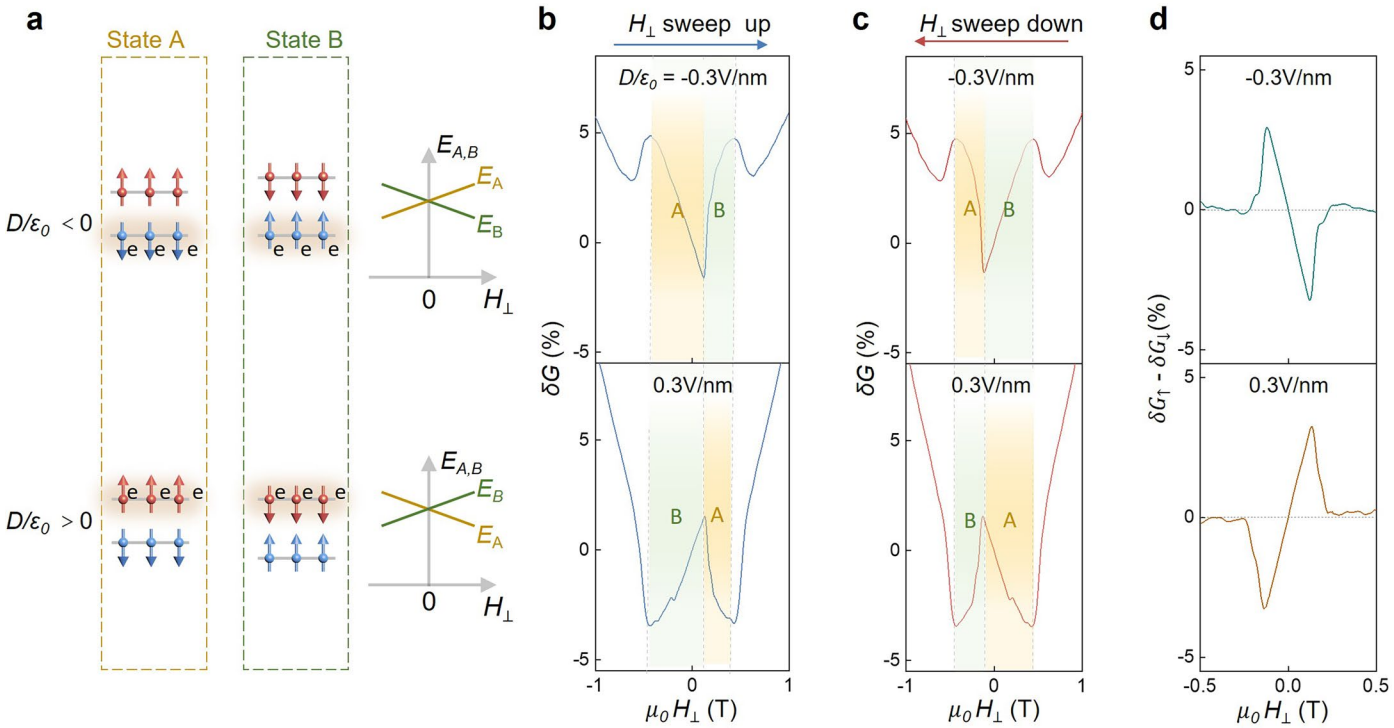

Extended Data Fig. 3 | Identification of states A and B in terms of a measurable quantity. a, At small magnetic fields, 2 L $CrPS_4$ can exist in two magnetic states, A and B, with opposite top and bottom layer magnetization. The spin polarization of gate-accumulated electrons (represented by the shaded region) follows the Cr atom magnetization, so that at finite D/ε_0 states A and B have different energies in the presence of a perpendicular magnetic field (Fig. 3). Here we show that the sign of $d(\delta G)/dH$ can be used to discriminate experimentally between the two states. **b**-**c**, Low-field magnetoconductance (δG) measured at 2 K at a constant electron density (1.5×10^{12} cm^{-2}) for opposite displacement fields, with the perpendicular magnetic field ($H_\perp$) swept up (**b**) and down (**c**). There is a univocal correspondence between the sign of the derivative of δG with respect to H (that is, $d(\delta G)/dH$) and whether the system is in state A or B. We label as 'A', the state when $d(\delta G)/dH < 0$ (yellow shaded areas in panels **b** and **c**), and as 'B' the state when $d(\delta G)/dH > 0$ (green shaded areas in panels **b** and **c**). Upon sweeping the magnetic field in different directions, and upon reversing the displacement field, the transitions between state A and B follow precisely the scheme outlined in panel **a**. For instance, in panel **a** for negative D, the bilayer undergoes a transition from state A to B when sweeping the magnetic field up, whereas for positive D the transition is from B to A. Panel **b** shows that this is precisely what we conclude by looking at the sign of $d(\delta G)/dH$. **d**, Magnetoconductance hysteresis ($\delta G_\uparrow - \delta G_\downarrow$) for opposite values of D/ε_0 (see legend). Based on the discussed logic, the opposite signs of the hysteresis under reversed displacement fields can be attributed to the reversed order of state switching Source data.

https://doi.org/10.1038/s41565-025-01872-w

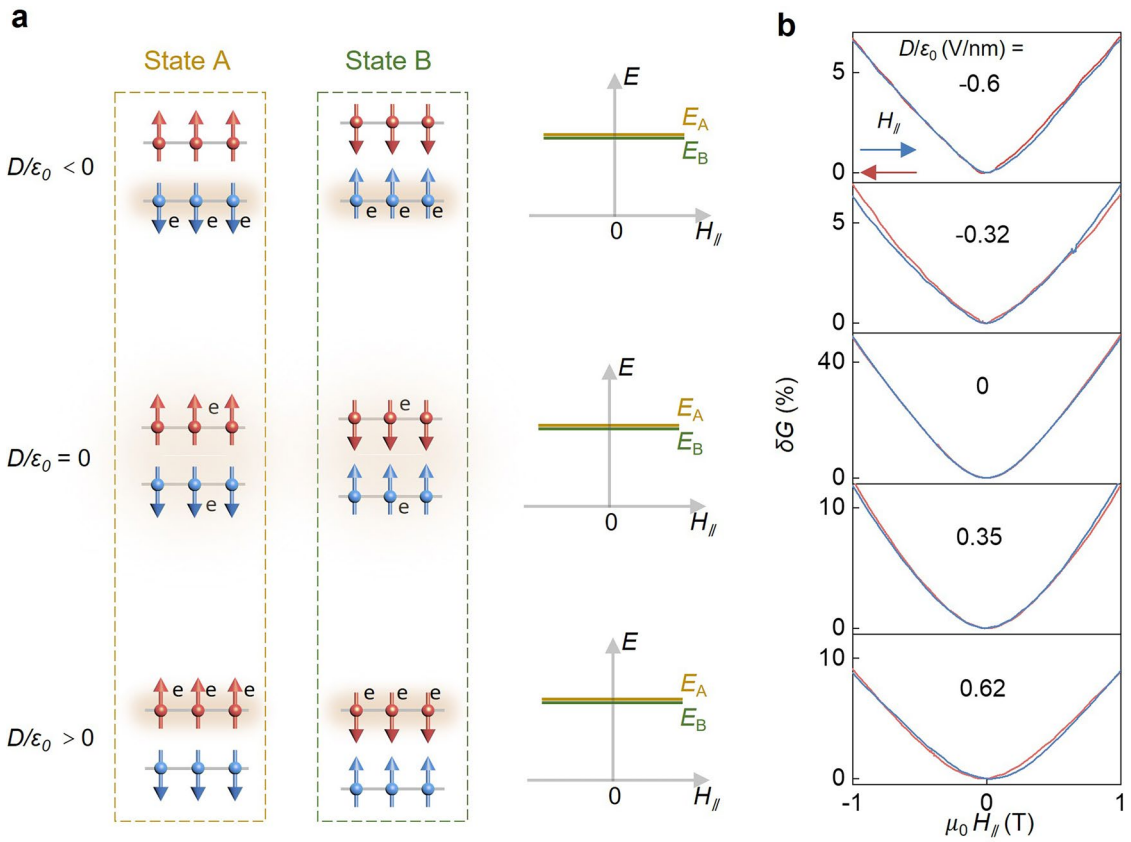

Extended Data Fig. 4 | Absence of hysteresis in the magnetoconductance under in-plane magnetic field. a, As discussed in the main text and above, at small magnetic fields 2 L $CrPS_4$ can be in one of two magnetic states, labelled A (left column) and B (middle column), where the magnetization of the top and bottom layers is opposite. The spin polarization of the electrons accumulated by the gate voltage (represented by the orange shadow) in each layer is determined by the magnetization of the Cr atoms in the same layer. When the magnetic field is applied perpendicular to the layers (as discussed in Fig. 3 of the main text), state A and B have different energy (at finite D/ε_0). However, when the magnetic field is applied parallel to the layers, the Zeeman energy of the electrons vanishes and state A and B always have the same energy. As a result, no hysteresis in the magnetoconductance is expected. **b**, Indeed δG measured at $T = 2$ K for different displacement fields (from top to bottom: −0.6 V/nm, −0.32 V/nm, 0 V/nm,0.35 V/nm, 0.62 V/nm) is independent of the direction in which the magnetic field is swept (the red (blue) trace represents the magnetoconductance measured as the field is swept up (down)), that is, no hysteresis is observed experimentally when the magnetic field is applied parallel to the plane, irrespective of the applied displacement field Source data.